Nano Energy 65 (2019) 104021

Contents lists available at ScienceDirect

Nano Energy

journal homepage: www.elsevier.com/locate/nanoen

Full paper

High-performing rechargeable/flexible zinc-air batteries by coordinated hierarchical Bi-metallic electrocatalyst and heterostructure anion exchange membrane

Nengneng Xu[a,f], Yanxing Zhang[c], Min Wang[a], Xiujun Fan[d], Tao Zhang[e], Luwei Peng[a], Xiao-Dong Zhou[f], Jinli Qiao[a,b,*]

[a] State Key Laboratory for Modification of Chemical Fibers and Polymer Materials, College of Environmental Science and Engineering, Donghua University, 2999 Ren'min North Road, Shanghai, 201620, China
[b] Shanghai Institute of Pollution Control and Ecological Security, Shanghai, 200092, China
[c] College of Physics and Materials Science, Henan Normal University, Xinxiang, Henan, 453007, China
[d] Institute of Crystalline Materials, Shanxi University, Taiyuan, 92 Wucheng Road, 030006, China
[e] State Key Lab of High Performance Ceramics and Superfine Microstructure, Shanghai Institute of Ceramics, Chinese Academy of Sciences, 1295 Dingxi Road, Shanghai, 200050, China
[f] Department of Chemical Engineering, University of Louisiana at Lafayette, Lafayette, LA, 70504, USA

ARTICLE INFO

Keywords:
Bifunctional catalyst
High power density
Rechargeable zinc-air battery
Flexible all-solid-state zinc-air battery
Wearable electronics

ABSTRACT

Due to the lack of highly efficient and low-cost oxygen reduction reaction/oxygen evolution reaction (ORR/OER) catalyst and alkaline anion exchange membrane (AEM), advanced rechargeable zinc-air batteries are largely hindered in many applications from wearable electronics to electric vehicles. Herein, a hybrid of porous Co_3O_4 anchoring on MnO_2, then interpenetrating with CNTs (Co_3O_4/MnO_2-CNTs) is synthesized via facile hydrothermal process, and an AEM (CS/EMImC-Co-EP/GO) employing semi-interpenetrating network structure is fabricated with a simple solution-casting method. The porous nanoparticles and chrysalis-like hybrid as well as strong bi-metallic coupling effect build highways and buffer zones for reactant and electrons transfer for ORR/OER. In addition, due to the competition of bottom Co atoms, the density functional theory (DFT) proves that the neighbor Mn sites (Mn1 and Mn2) of the MnO_2(110) surface are evidently activated, which prompts the catalytic activity of hybrids by making the Mn1, Mn2 3d density of states move forward lower energy entirely. As a result, Co_3O_4/MnO_2-CNTs exhibit superior ORR/OER activities with the low potential difference (ΔE) of 0.85 V and impressive performances in rechargeable aqueous zinc-air batteries (power density: 534 mW cm^{-2}). Moreover, combining AEM integrated into rechargeable flexible all-solid-state zinc-air batteries and stack, the enhancement natures of wearable devices are achieved even under different bending angles benefiting from high hydroxyl anion conductivity and remarkable flexibility of AEM semi-interpenetrating network, which accelerates ion transport by the synergy of hopping and vehicle mechanisms. Furthermore, the flexible all-solid-state zinc-air batteries show excellent tolerance toxicity of CO_2.

1. Introduction

Thanks to the high energy density, environmental benignity as well as good reliability, flexible rechargeable zinc-air batteries receive tremendous interest in next-generation electrochemical energy storage and conversion devices, such as roll-up displays, flexible cell phones and intelligent bracelet [1–7]. Unfortunately, flexible rechargeable zinc-air batteries still face two challenges [8,9]: developing highly efficient bifunctional catalysts to improve the slow speed of the oxygen reduction and oxygen evolution reactions (ORR and OER, respectively), and exploiting high-performance solid-state electrolyte to promote the unusual omnidirectional flexibility [10–12]. For the first challenge, Co/Mn-based material as a promising bifunctional catalysts candidate alternative to precious metal catalysts (such as Pt, Ir and their alloys) have been rapidly developed over recent years [13,14], because of the low cost, abundant valence states, and satisfactory electrochemical

* Corresponding author. State Key Laboratory for Modification of Chemical Fibers and Polymer Materials, College of Environmental Science and Engineering, Donghua University, 2999 Ren'min North Road, Shanghai, 201620, China.
E-mail address: qiaojl@dhu.edu.cn (J. Qiao).

https://doi.org/10.1016/j.nanoen.2019.104021
Received 12 April 2019; Received in revised form 12 July 2019; Accepted 13 August 2019
Available online 19 August 2019

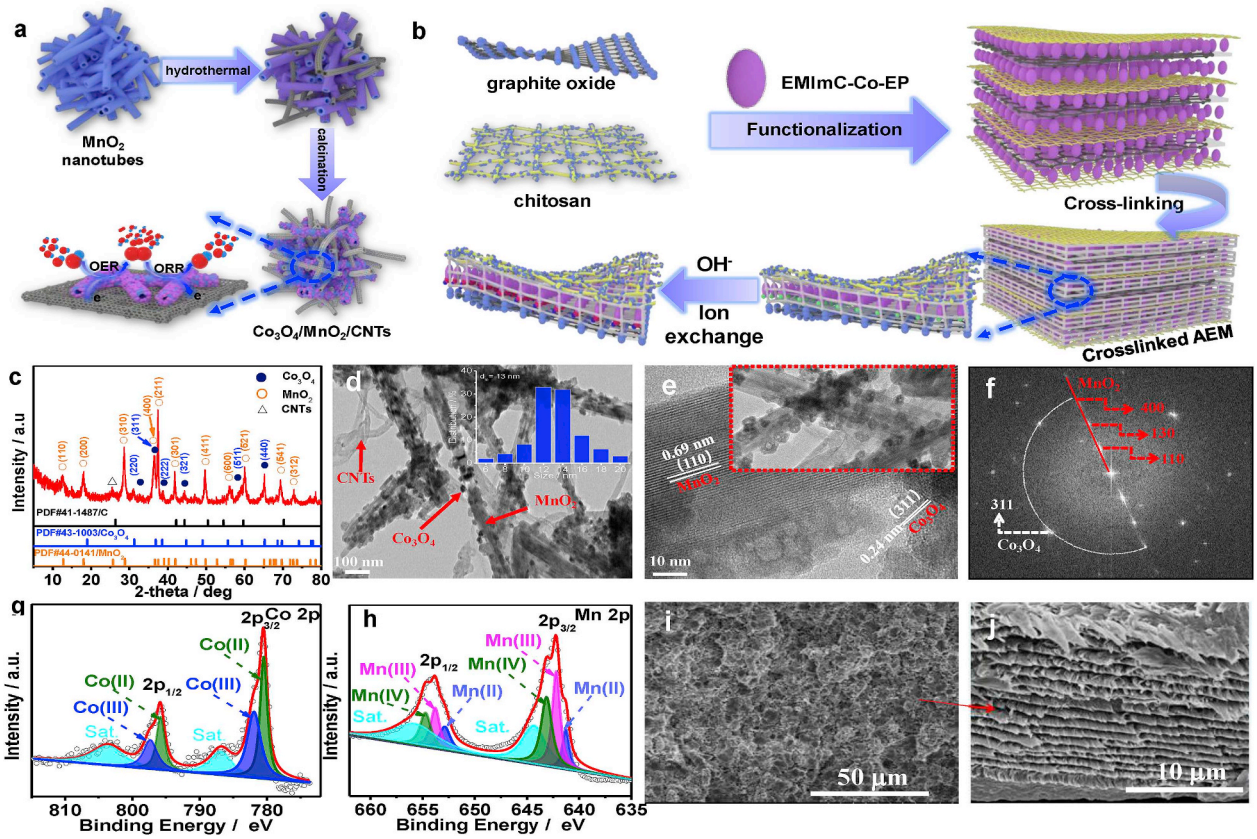

Fig. 1. (a–b) Illustrations of the preparation of the Co_3O_4/MnO_2-CNTs hybrid catalyst and GO-Chitosan/EMImC-Co-EP alkaline anion-exchange membranes, respectively. (c–d) XRD pattern and TEM image of the Co_3O_4/MnO_2-$CNTs_{350}$ hybrid nanomaterials. (Insert of d: Particle size distribution of Co_3O_4 nanoparticles in Co_3O_4/MnO_2-$CNTs_{350}$); (e) HRTEM image of Co_3O_4/MnO_2-$CNTs_{350}$ hybrid catalyst (Insert: part of the amplification of TEM image); (f) FFT pattern of Co_3O_4/MnO_2-$CNTs_{350}$ in the hybrid; XPS spectrum of Co_3O_4/MnO_2-$CNTs_{350}$ (g) Co 2p region; (h) Mn 2p region; (i and j) SEM image of 1 wt%GO and Polymer composition: Chitosan/EMImC-Co-EP = 1:0.75 by mass.

properties [15–17]. Specifically, the hybrid catalysts of MnO_2-CNTs and Co_3O_4-CNTs [17] were widely studied and exhibited decent activities towards ORR and OER in alkaline mediums. In spite of these tremendous outcomes, it remains great challenge regarding the following aspects on the Co/Mn-based materials: i) the Co/Mn oxides catalysts are still need to optimize to meet the high conversion efficiency requirements for the zinc-air batteries [18–20]; ii) Hierarchical nanostructures with irregular chrysalis-like sphere featuring high surface area, abundant active sites, and favorable interpenetrating electron transfer pathway are still lacking [2,13]. Generally, the ORR and OER catalystic behaviors of Co/Mn-based hybrid materials could be directly enhanced through optimization of morphological architecture, surface configuration, and electronic/defective Engineering [1,21,22]. Therefore, for a given catalyst, precise composition control and rational morphology engineer are efficient strategies to boost the performance of oxygen electrode.

For the second challenge, there are two avenues for preparing solid-state electrolytes. One is incorporating alkaline liquid into inert gel polymer matrix (i.e., PVA membranes), which exhibits high hydroxide-ion capacity by facilitating the kinetic reactions of flexible batteries [8,23,24]. Unfortunately, the high hydrophilicity of gel polymer makes it difficult to provide sufficient flexibility and safety [23]. Meanwhile, the gel electrolyte progressively releases the incorporated alkaline liquid, which causes a large ohmic polarization and further damages the batteries' stability. Compared with the gel polymer matrix, the anion-exchange membranes (AEMs) importing OH^- functional groups into polymer backbone have been widely used in fuel cells and show a great promise in flexible zinc-air batteries [9,25,26]. In zinc-air battery, the AEMs directly prevent the migration of zinc ion and formation of carbonate during battery operations, improving the durability. However, the water-retaining property of traditional membranes is relatively poor, and directly limits the discharge process of flexible rechargeable zinc-air batteries. In addition, the membranes tend to lose water rapidly by evaporation owing to the open system. Particularly, the ionic conductivities of membranes strongly rely on the degree of hydration and ion-exchange capacities, which limit the battery performance. Therefore, all-solid-state electrolytes based on graphene oxide (GO) have been intensely studied due to the outstanding physicochemical stability and abundant oxygen-containing groups of GO [25]. However, the above-mentioned membranes are diminished with the difficulty to form a mechanically robust membrane, making the free-standing GO membranes less attractive for being used as practical solid-state electrolytes. To enhance the mechanical strength, several fillers can be incorporated into the GO layer. Among the multifarious materials, chitosan as fire-new renewable material is recognized as a good binder and surface modifier due to its high hygroscopicity, flexibility, large surface area-to-volume ratio together with porous substrate [26]. Specially, owning to the rich hydroxyl groups, chitosan can be easily refashioned through a surface-functionalization to conduct ions and be utilized in flexible batteries. Therefore, engineering of interpenetrating conjunction between the chitosan and GO is vital to enhance the conductivity, flexibility and mechanical strength, but has yet to be achieved.

Herein, a novel chrysalis-like bifunctional catalyst with homogeneous porous Co_3O_4 nanoparticles distributed on the surface of MnO_2 (Co_3O_4/MnO_2-CNTs) was synthesized by elaborately modulating the advantageous structure and morphology. Simultaneously, an efficient and ultra-flexible electrolyte membrane with unique three-dimensional

semi-interpenetrating network was developed by a simple solution-casting method. The as-prepared Co_3O_4/MnO_2-CNTs create buffer zones, accelerating separation of products on the catalyst surface, which provide a thermodynamically favorable environment for ORR and OER. Particularly, the surface Mn1 and Mn2 atoms get little electrons by the transfer of Co_3O_4, further decreasing the hydrogen bonding and accelerating the ORR and OER. As expected, Co_3O_4/MnO_2-CNTs exhibited admirable electrocatalytic activity for both ORR and OER with low potential gap ($\Delta E = E_{OER}-E_{ORR}$) of 0.85 V, and possessed remarkable single- and stack-batteries performances, which surpasses that of IrO_2 and Pt/C as noble metal benchmarks. Meanwhile, due to the 3-D semi-interpenetrating network structure and the synergistic effect of jumping mechanisms and rolling mechanisms, the all-solid membrane displays remarkable ion-exchange capacities and the water-retaining property. In particular, the flexible zinc-air batteries with CS/EMImC-Co-EP/GO solid electrolyte and Co_3O_4/MnO_2-CNTs air electrodes are developed. The flexible all-solid-state zinc-air batteries exhibit excellent power density (83.5 mW cm^{-2}), high specific capacity (~600 mAh g^{-1}), outstanding stability (35 h), flexibility and excellent tolerance toxicity of CO_2. The flexible zinc-air battery stack also shows high working voltage and excellent charge-discharge cycles stability, which further enlarges the application scope of the flexible battery.

2. Experimental section

2.1. Synthesis of Co_3O_4/MnO_2-CNTs hybrid cathode catalyst

The synthesis procedure for the Co_3O_4/MnO_2-CNTs involves three steps (Fig. 1a). First, the MnO_2 nanotubes were synthesized by a simple hydrothermally treated at 140 °C for 12 h [17]. Second, 0.2 g of Co $(NO_3)_2$ $4H_2O$, 0.2 g MnO_2 nanotube and 0.125 g CNTs were dispersed in 30 mL of 1.3 mol L^{-1} ammonia solution. The mixture was transferred into a 100 mL autoclave and maintained at 160 °C for 6 h. The collected powder was separated by several centrifuge-wash cycles with deionized water and ethanol, and then dried at 60 °C for 12 h. The second-step desiccative powder was calcined in air at 200, 300, 350, 400 and 500 °C for 1 h to obtain the final product (denoted as Co_3O_4/MnO_2-$CNTs_{200}$, Co_3O_4/MnO_2-$CNTs_{300}$, Co_3O_4/MnO_2-$CNTs_{350}$, Co_3O_4/MnO_2-$CNTs_{400}$ and Co_3O_4/MnO_2-$CNTs_{500}$, respectively).

2.2. Synthesis of CS/EMImC-Co-EP-OH/GO membranes

The membranes were prepared with a solution-casting method, where 1 g chitosan (CS) was dissolved in 50 mL acetic acid solution (2 wt%) and stirred until complete dissolution. 1-Ethenyl-3-methyl-1Himidazoliumchloride polymer with 1-ethenyl-2-pyrrolidone (EMImC-Co-EP) was separately prepared, and then EMImC-Co-EP, CS (the CS/EMImC-Co-EP = 1:0.75 by mass) and a certain amount of 2 ml g^{-1} graphite oxide (GO) solution were mixed with different proportions under stirring overnight to get a homogeneous appearance. The final resulting solution was poured into the plastic dishes and dried in the ambient conditions. Membranes were obtained with a thickness of ~ 75 μm. Before use, the samples were heated at 140 °C for 1 h, then soaked in a reaction solution containing 10 mass% glutaraldehyde (GA) in acetone for chemical cross-linking with a small amount of hydrochloric acid as a catalyst for 1 h. The membranes were rendered conducting by immersion of CS/EMImC-Co-EP/GO membranes into 2 M KOH and equilibrated for 24 h to convert it from Cl^- into OH^- form (Fig. 1b).

2.3. Materials characterization

The microstructural characteristics of these samples were recorded by field-emission scanning electron microscope (FESEM) (FEI Sirion 200) and high-resolution transmission electron microscope (HR-TEM) (JEOL JEM-2100F). The spinel crystal structures of the hybrid samples were verified by X-ray diffraction (XRD) (Bruker AXS D8 Advance). Meanwhile, X-ray photoelectron spectroscopy (XPS) data were obtained by a Theta Probe electron spectrometer from Thermo Scientific. Fourier transforms infrared (FTIR) spectroscopy was used to study the molecular structure of CS/EMImC-Co-EP/GO membranes. The infrared spectrometer (Tensor 27, Bucker) equipped with attenuated total reflectance (ATR) instrument was used to obtain the spectrogram. The gravimetric analysis (TG) of membranes was carried out with a TG 209 analyzer (Netzsch).

2.4. Aqueous/flexible rechargeable zinc-air batteries/stack preparation and tests

The air electrode was prepared by spray-coating the catalyst ink solution onto a gas diffusion layer (GDL, Toray TGP-H-090, active area of 4 cm^2 and catalyst loading: 2 mg cm^{-2}). A rechargeable zinc-air battery was fabricated using the as-prepared air-cathode, zinc plate as anode, and 6 M KOH solution as electrolyte. The aqueous zinc-air battery stack was assembled by pressing three the single aqueous zinc-air cell. The single flexible zinc-air battery was assembled through face-to-face method, in which the CS/EMImC-Co-EP/GO membrane was paired with a zinc foil electrode and a bifunctional air electrode with commercial Co_3O_4/MnO_2-$CNTs_{350}$ deposited on a nickel foam. And the battery using the commercial Tokuyama A901 anion-exchange membrane was also fabricated for the comparison. The assembled device was pressed under a pressure of 3 MPa for 2 min by a sheeting presser to enhance its integrity of the laminated structure. Briefly, Copper (Cu) foil as a substrate is attached to the zinc electrode (thickness: 0.03 mm). The novel air electrode was prepared by spray-coating the catalyst ink solution onto a nickel foam (GDL, Toray TGP-H-090, active area of 4 cm^2 and catalyst loading: 2 mg cm^{-2}). The flexible zinc-air battery stack was assembled by pressing three the single flexible zinc-air cell. The discharge polarization and power density plots were obtained using a galvanodynamic method. Battery cycling experiments were performed using the recurrent galvanic pulse method with a constant current density and time.

3. Result and discussion

To obtain the crystal structure of Co_3O_4/MnO_2-$CNTs_{350}$, the XRD measurement of the hybrid was carried out. As shown in Fig. 1c, the characteristic peak located at 26° corresponds to the (002) plane of CNT (JCPDS file no. 41–1487), and other characteristic peaks correspond to the planes of Co_3O_4 (JCPDS file no. 43–1003) and MnO_2 (JCPDS file no. 44–0141), suggesting the successful synthesis of Co_3O_4/MnO_2-$CNTs_{350}$. As displayed in FESEM images (Fig. S1), Co_3O_4/MnO_2-$CNTs_{350}$ shows an irregular chrysalis-like sphere with an average size of 5–20 μm. In the hierarchical nanostructures, the homogeneous Co_3O_4 nanoparticles densely anchored on surface of MnO_2, forming a mosaic-structure Co_3O_4/MnO_2 hybrid. The Co_3O_4/MnO_2 then intertwined with CNTs forming a chrysalis-like nanostructure, greatly promoting the transfer of electron coming from oxygen reaction on the surface of Co_3O_4/MnO_2. Meanwhile, CNTs can restrain the accumulation of Co_3O_4/MnO_2. Also, the annealed sample provided a cross-linked network to further prevent the decomposition of these oxide particles. The conductive channels facilitate electrolyte permeation and buffers to accommodate volume changes of air electrode during charge and discharge processes. The precise morphology information of the catalyst was verified by TEM and HRTEM images (Fig. 1d and e). As shown in Fig. 1e, lots of 3D porous Co_3O_4 nanoparticles with an average particle size (dm) of 13 nm (size: 6–20 nm, Fig. 1d **inset**) are uniformly anchored on MnO_2 nanotubes (Fig. S2a-**c**). The atomic percentage of Co, Mn, C, O and Cu are 5.1%, 22%, 14.3%, 50% and 8.6%, respectively (the Cu comes from copper mesh substrate, Fig. S2d). The porous structure (Fig. 1e **inset**) may stems from the kirkendal effect, which release H_2O and CO_2 during the calcination. The processes can be

written as reaction 1 and reaction 2:

$$Co(OH)_2 \rightarrow Co_3O_4 + H_2O\ (g) \quad (1)$$

$$C + O_2 \rightarrow CO_2 \quad (2)$$

The N_2 adsorption/desorption isotherm curve (Fig. S1d) of the hybrid exhibits the typical porous feature (IV type) with an ultra-high Brunauer-Emmett-Teller (BET) surface area of 801 $m^2 g^{-1}$. The average diameter of the mesoporous is calculated to be about 3–5 nm (**inset** of Fig. S1d). The hybrid catalyst features high specific surface area, which should be attributed to the porous nanoparticles and the unusual chrysalis-like nanostructure. These unique characteristics provide abundant exposed active sites, shorten the reactants diffusion paths and promote mass/charge transfer [17]. Further from the HRTEM images of Co_3O_4/MnO_2-CNTs (Fig. 1e), the lattice spacings of 0.69 and 0.24 nm correspond to the (110) plane of a-MnO_2 and (311) plane of Co_3O_4, respectively [17,27,28]. And the Fourier Transform Algorithm (FFT) pattern (Fig. 1f) give more diffraction spots characteristic of the Co_3O_4/MnO_2-CNTs hybrid, which agree well with the XRD results (Fig. 1c).

To reveal the chemical state and elemental composition in the Co_3O_4/MnO_2-$CNTs_{350}$ hybrid, XPS measurements are carried out and the corresponding results are displayed in Fig. S1. The spectrum of Co *2p* can be deconvoluted into two spin-orbit doublets and two shakeup satellites (denoted as "sat", Fig. 1g). Especially, two pairs of $2p_{3/2}$-$2p_{1/2}$ doublets are assigned to Co^{2+} (780.2/795.6 eV) and Co^{3+} (782.5/797.8 eV) with an energy separation of 15.3 eV [28–32]. Fig. 1h reveals the high-resolution XPS spectrum of Mn *2p*. The main peaks are centered at 642.3 and 654.1 eV with a spin energy separation of 11.8 eV, which are in good agreement with Mn ($2p_{3/2}$) and Mn ($2p_{1/2}$) in MnO_2 [33,34]. The O 1s spectrum (Fig. S1f) can be deconvoluted into three peaks at 530.0, 531.2 and 532.7 eV, which corresponds to lattice oxygen, surface adsorbed oxygen and surface adsorbed water molecules, respectively [32,35]. The hybrid presents the highest peak intensity of Oad among all peaks, illustrating the presence of more oxygen defects. Fig. S1g presents the deconvoluted C 1s spectra which shows four kinds of C species, including the C=C at 284.1 eV, C–C at 284.6 eV, C–OH at 285.3 eV, and O=C–O (287.8 eV) [29,36]. The ORR and OER catalytic activity of the hybrid can be attributed to the mixed valences of coexisting Mn and Co cations, which accelerate electron transfer by supplying donor-acceptor chemisorption sites for both reversible oxygen desorption and adsorption.

Specifically, the morphology and physicochemical characteristic of the hybrid was converted with the change of calcination temperature. Hence, the physicochemical characteristics of the hybrid were studied by performing BET surface area, XRD patterns, TEM and XPS spectrum. As expected, the morphologies, crystallinity and chemical composition of the synthesized Co_3O_4/MnO_2-$CNTs_x$ are temperature dependent (Figs. S3–9). As the temperature increased, the crystallinity of the catalyst increased and the cobalt compounds tended to form a certain shape Co_3O_4 by further dehydration (Fig. S3). CNTs were also partly oxidized, which might play the role in forming pores. Concretely, at 200 °C, less Co_3O_4 (dm = 7.5 nm) anchored on MnO_2 nanotubes surface, while the CNTs and Co_3O_4/MnO_2 are almost in their separate states (Fig. S4). At 300 °C, more Co_3O_4 nanoparticles (dm = 5 nm) are aggregated on the surface of MnO_2 nanotubes and the shape of MnO_2 nanotubes becomes more evident and regular (Fig. S5). Further increasing the calcination temperature to 400 °C, Co_3O_4 nanoparticles (dm = 14.5 nm) with 6–7 nm of circular porous structure, MnO_2 nanotubes, and CNTs are in a uniformly hybrid state and the amount of CNTs began to decrease (Fig. S6). At 500 °C, the CNTs in the mixed catalyst are almost disappeared, resulting the destruction of the regular form of MnO_2 nanotubes, and the Co_3O_4 nanoparticles still maintain the same morphology with dm of 19.5 nm (Fig. S7). Since the fast dehydration at high calcination temperature (ie., 400 °C), the Co_3O_4 nanoparticles are quickly formed and aggregated randomly on the surface of MnO_2 nanotubes/CNTs hybrid, thus some hollow structures are destroyed. Correspondingly, all Co_3O_4/MnO_2-$CNTs_x$ composites exhibit combined characteristics of type IV isotherms, suggesting the existence of micro-pores. The BET surface area of Co_3O_4/MnO_2-$CNTs_x$ increases from 32 to 801 $m^2 g^{-1}$ as the pyrolysis temperature increased from 200 to 350 °C, but decreases to 134 $m^2 g^{-1}$ and 48 $m^2 g^{-1}$ at 400 and 500 °C, respectively, which probably can be attributed to the decline of amount of CNTs and the reunion Co_3O_4 nanoparticles. N_2 sorption results also show that the calcination temperature has a significant effect on the porous structures of the obtained materials which exhibit different pores size, which agree well with the TEM results. Moreover, there was significant change in the chemical valence state of the catalyst synthesized with different temperature (Fig. S9). Hence, the above-mentioned results reveal the superiority of the proposed temperature for providing a forming unique size, structure and electronic valence, which facilitate oxygen transportation and promote the catalytic reaction.

Fig. 1i and j show the cross-view SEM images for CS/EMImC-Co-EP membranes with 1% GO. After GO doping, the CS/EMImC-Co-EP film possesses internal three-dimensional structure with semi-interpenetrating network. GO chains are well embedded in and constitute the network structure, making the internal more closely. The addition of GO can effectively improve the material nature inside the membrane link, further enhance the stability and mechanical strength of the membrane, which agree well with the FTIR spectra results (Fig. S10). And the mechanical properties of composite membranes were tested and concluded in Table S1. The CS/EMImC-Co-EP/GO membranes with moderate content of GO (1 wt% GO) afford the maximum tensile strength of 33.63 MPa, Young modulus of 720 Mpa and elongation at break of 9.77%. The result directly demonstrates that GO greatly improved the tensile strength, elongation and Young's modulus of the membrane.

The ORR and OER performance of engineered catalysts (Co_3O_4/MnO_2-$CNTs_x$) were measured in 0.1 M KOH, as well as two commercial IrO_2 and Pt/C catalysts as benchmark for comparison (Fig. 2a and b and Fig. S11). Co_3O_4/MnO_2-$CNTs_{350}$ exhibits high ORR activity and with relatively decent half-wave potential and limiting current density (Fig. 2a and Fig. S11a). Co_3O_4/MnO_2-$CNTs_{350}$ affords a more positive onset potential of 0.97 V at current density 0.1 mA cm^{-2} than that of IrO_2 (0.81 V) and Co_3O_4/MnO_2-$CNTs_x$ (x = 200, 300, 400 and 500), and onset potential value even is essentially competing with that of Pt/C (0.97 V), Fig. S12 shows the ORR polarization curves for Co_3O_4/MnO_2-$CNTs_x$ at different rotation rates (300–1500 rpm) and the corresponding Kouteckye-Levich plots obtained at 0.3034 V, 0.3534 V, 0.4034 V, 0.4534V and 0.5034V, respectively [37]. The electron-transfer number (n) during ORR was calculated to be in the range of 3.93–3.95, which is similar to that of Pt/C (3.98) and larger than others catalysts (Co_3O_4/MnO_2-$CNTs_{200}$: 3.25, Co_3O_4/MnO_2-$CNTs_{300}$: 3.90, Co_3O_4/MnO_2-$CNTs_{400}$: 3.85 and Co_3O_4/MnO_2-$CNTs_{500}$: 3.11), suggesting that the ORR proceeds via a four-electron-transfer scheme involving the in situ OH^- formation in alkaline medium. As illustrated in Fig. 2b and Fig. S11b, the OER activity of the Co_3O_4/MnO_2-$CNTs_{350}$ hybrid catalyst is outperformed by Co_3O_4/MnO_2-$CNTs_{200,\ 300,\ 400\ and\ 500}$, Pt/C and IrO_2. And the hybrid catalyst shows a high OER current density of 45 mA cm^{-2} at 2.0 V, which are much higher than Co_3O_4/MnO_2-$CNTs_{200}$ (15.3 mA cm^{-2}), Co_3O_4/MnO_2-$CNTs_{300}$ (24.9 mA cm^{-2}), Co_3O_4/MnO_2-$CNTs_{400}$ (24.0 mA cm^{-2}), Co_3O_4/MnO_2-$CNTs_{500}$ (26.2 mA cm^{-2}), IrO_2 (9.8 mA cm^{-2}) and Pt/C (8.7 mA cm^{-2}). The potential difference (ΔE) between E_{ORR} at a current density of 3 mA cm^{-2} and E_{OER} at a current density of 10 mA cm^{-2} is a key parameter to evaluate the catalytic bifunctionality [38,39]. A higher bifunctionality for catalyzing ORR and OER is closely related to a low value of ΔE [40,41]. Fig. 2c displays a detailed comparison of this work and recently reported bifunctional oxygen catalysts. As expected, the activity of Co_3O_4/MnO_2-$CNTs_{350}$ ranks among the highest level. The Co_3O_4/MnO_2-$CNTs_{350}$ shows the minimum value of ΔE (0.85 V) among these catalyst, including Pt/C (1.18 V), IrO_2 (1.51 V), Co_3O_4/MnO_2-$CNTs_{200}$ (1.41 V), Co_3O_4/MnO_2-$CNTs_{300}$ (1.06 V), Co_3O_4/MnO_2-$CNTs_{400}$ (1.02 V), $Co_3O_4/$

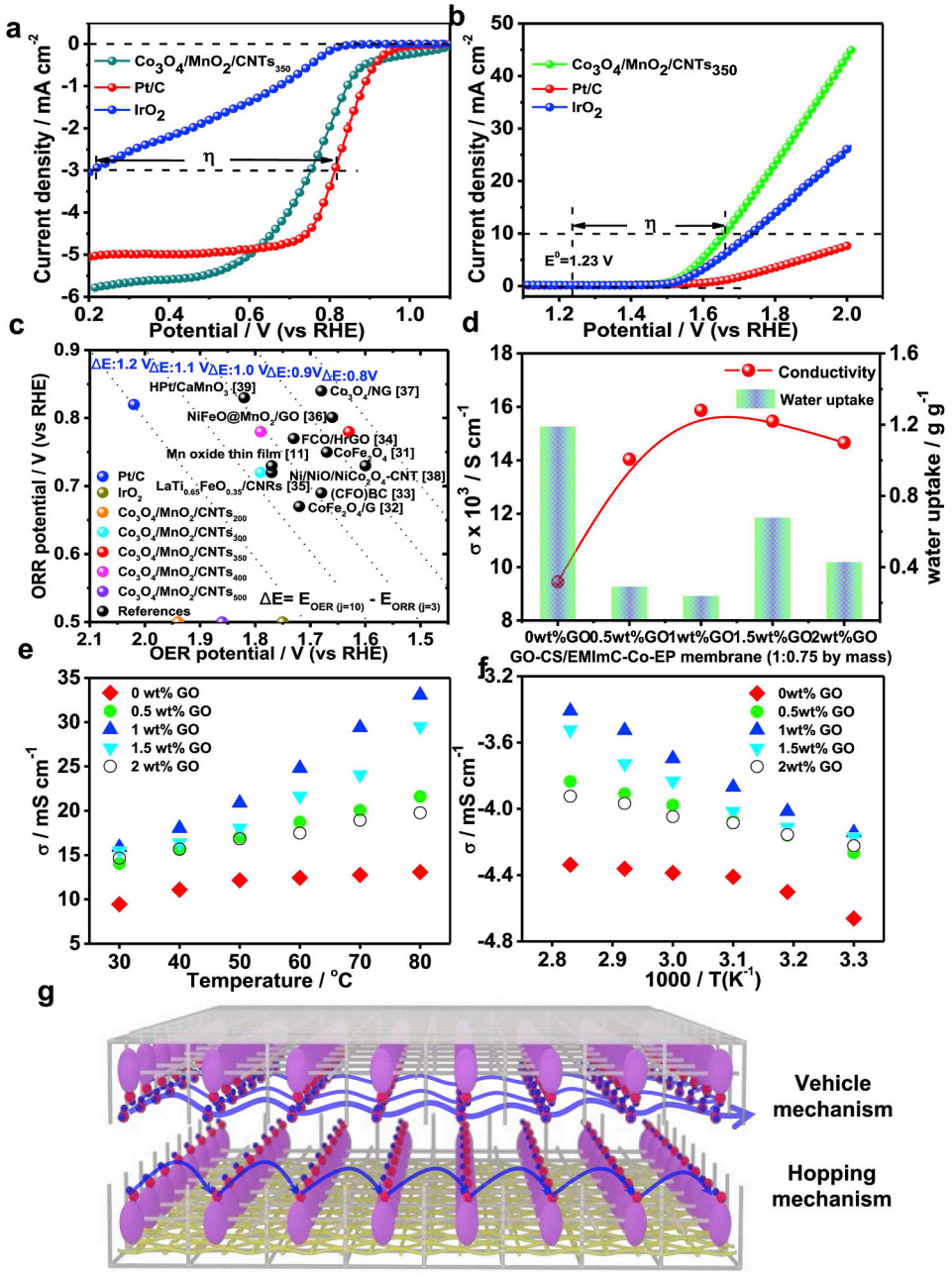

Fig. 2. (a) ORR polarization curves of Co_3O_4/MnO_2-$CNTs_{350}$, Pt/C, and IrO_2; (b) OER polarization curves of Co_3O_4/MnO_2-$CNTs_{350}$, Pt/C, and IrO_2; (c) Comparison of OER and ORR bifunctional activities of samples in this work with representative catalysts in references; (d) OH^- conductivity and WU of Chitosan/EMImC-Co-EP alkaline membranes in the different content of GO; (e) Temperature dependence of OH^- conductivity; (f) the log(σ) vs. 1000/T plot for Chitosan/EMImC-Co-EP alkaline membranes in the different content of GO; (g) Illustration of jumping and rolling mechanisms of Chitosan/EMImC-Co-EP alkaline membranes.

MnO_2-$CNTs_{500}$ (1.06 V) and among the most recently reported catalyst [42–52]. The high activity of the hybrid could be ascribed to hybridization strategy that existing the unique morphology of the spinel-CNTs with, which provide/activate more active sites, abundant oxygen transportation channel and unusual electron conduction network. As the temperature ranges from 200 °C to 350 °C, the activity of the catalyst was slowly increased. The catalyst activity decreased rapidly as the temperature increased from 400 to 500 °C, and especially at 500 °C. This phenomenon can be attributed to the formation/reunition process of porous Co_3O_4 nanoparticles (Fig. S3) and the large decline of CNTs in the mixed catalyst (Fig. S7 and Fig. S9a), worsing electrical conductivity of the hybrid catalyst. However, the morphology of Co_3O_4 nanoparticles is still maintained in the Co_3O_4/MnO_2-CNTs composites with larger in size. All findings further indicate that the particle sizes, the porous structure, the preferentially (110) facets, and the bimetal synergistic coupling effect of the hybrid are important for the overall catalytic activity. These inherent characteristic of the hybrid create abundant buffer zones, accelerate separation of products on the catalyst surface and provide a thermodynamically favorable environment for ORR and OER, which will be further demonstrated by the density functional theory (DFT) Semi-core Pseudopotentials (DSPP) calculations. In addition, CNTs have an important role in the formation of the catalyst pores and promote the conductivity and activity of the catalyst. The CNTs with a well-defined structure in the Co_3O_4/MnO_2-CNTs composites facilitate the electron transfer trough the inner walls, while the outer walls can be as a base for supporting the metal oxides. Herein, the ORR and OER are rapidly occurred on metal oxide surfaces, and the obtained electrons are transferred by CNT network (Fig. 1a). While, exact identification of the contribution of all the feasible mechanisms mentioned above is beyond the

range of this work.

In order to explore the effect of GO doping on the CS/EMImC-Co-EP basic anion exchange membrane, the OH^- conductivity (σ_{OH^-}) and water uptake (WU) of CS/EMImC-Co-EP/GO were tested (Fig. 2d), where the CS/EMImC-Co-EP/GO mass ration ranged from 0 wt% to 2 wt% by mass. Compared with CS/EMImCCo-EP/GO without GO, the σ_{OH^-} of the membrane with 1 wt% GO increased by 40%, then reached a plateau of 0.016 S cm^{-1}. At the same time, the WU was reduced to a minimum. The (σ_{OH^-}) varies from (16–33) × 10^{-3} S cm^{-1} in D.I. water within the temperature range of 30–80 °C (Fig. 2e). Here, membranes exhibited an increment in ionic conductivity with the temperature increasing, which is attributed to two reasons: (i) faster thermal and diffusion motion of OH^- are expedited at raised temperatures, thus reducing the activation energy for ion transport [53] and (ii) the membraned main chains will further provide a larger free volume to enhanced ion transport by increasing in flexibility at raised temperatures [54]. The mechanical property of Chitosan/EMImC-Co-EP/GO was also obtained (Table S1). Fig. 2f further shows the Arrhenius plots of membranes, it can be seen that the calculated apparent activation energies (E_a) fall into the range from 5.34 to 13.50 kJ mol^{-1} for all CS/EMImC-Co-EPOH/GO membranes. This is similar to that of CS/EMImC-Co-EP/GO without GO (5.35 to 11.56 kJ mol^{-1}), which indicates that there are two mechanisms of jumping and rolling, and the former is more dominant (Fig. 2g).

To validate the excellent bifunctional activity of the Co_3O_4/MnO_2-$CNTs_{350}$ catalyst, a conventional home-made zinc-air battery is assembled to further identify its performance under real battery operation conditions (air, Fig. 3a). As displayed in Fig. 3b and Fig. S13a, the battery with Co_3O_4/MnO_2-$CNTs_{350}$ hybrid materials as cathode catalyst delivers a higher open circuit voltage (OCV) of 1.45 V, which is higher than that of Pt/C (1.41 V) and Co_3O_4/MnO_2-$CNTs_x$ (x = 200, 300, 400 and 500). Moreover, Co_3O_4/MnO_2-$CNTs_{350}$ cathode catalyst gives a high discharge peak power density of 534 mW cm^{-2}, which is superior to Pt/C (127 mW cm^{-2}), Co_3O_4/MnO_2-$CNTs_x$ (x = 200, 300, 400 and 500) and some recently reported literature (Table S2). Additionally, Fig. S13b displays the discharge curves at the various current densities (5 mA cm^{-2} to 50 mA cm^{-2}, Δj = 2.5 mA cm^{-2}), keeping 3 h at each current density, then return to 5 mA cm^{-2} for 3 h. These each step discharge curves of Co_3O_4/MnO_2-$CNTs_{350}$ are more smooth and stable than other catalysts. It is particularly noteworthy that the working voltage can still reach the initial state when the current density is back to 5 mA cm^{-2}. The long time discharged voltage (> 1V) maintain more than 200 h than Pt/C (120 h) and Co_3O_4/MnO_2-$CNTs_x$ (x = 200, 300, 400 and 500) at a current density of 10 mA cm^{-2}, which proves the outstanding stability of the Co_3O_4/MnO_2-$CNTs_{350}$ cathode catalyst for ORR (Fig. 3c and Fig. S13c). The voltage loss is in fact associated with the degradation of zinc anode [55]. The specific capacity normalized to the mass of consumed Zn (≈2.85 g) was ~770 mAh g^{-1} and corresponding to energy density was > 842 Wh kg^{-1}, which are better than that of Pt/C (450 mAh g^{-1} and 490 Wh kg^{-1}) and Co_3O_4/MnO_2-$CNTs_x$ (x = 200, 300, 400 and 500) (Fig. S12d). In order to further investigate the performance of the rechargeable zinc-air batteries, charge and discharge (C-D) polarization curves tests and galvanostatic discharge-charge cycling tests were carried out, as shown in Fig. 3d and Figs. S13e–f and Fig. S11. To obtain a meaningful comparison, a commercial Pt/C was used for rechargeable battery measurements. Fig. S13e and Fig. S14 show typical C-D polarization curves, the difference value of the whole C-D voltage of the Co_3O_4/MnO_2-$CNTs_{350}$ cathode is 1.5 V at a current density of 70 mA cm^{-2} lower than that of Pt/C (1.47 V) and Co_3O_4/MnO_2-$CNTs_x$ (x = 200, 300, 400 and 500). It shows that the Co_3O_4/MnO_2-$CNTs_{350}$ catalyst is suitable for high power density device, to meet the development trend in the future. Fig. 3d shows a typical charge-discharge cycling, the initial discharge and charge voltages are about 1.2 and 2.09 V at a current density of 20 mA cm^{-2} for 10 min per cycle, respectively, and the voltage gap is only about 0.89 V. The voltage maintains very well for both discharge and charge; small drop (0.36 V) is observed after continuous cycling of more than 135 h (up to 810 cycles). But the rechargeable zinc-air battery with a Pt/C cathode shows notable changes after 20 h. In order to further illustrate the charging and discharging performance of the catalyst, a large current density charge-discharge cycling (50 mA cm^{-2}) was executed (Fig. S13f). The charge-discharge voltage drop (1.2 V) maintains no visible change more than 110 h and superior to Co_3O_4/MnO_2-$CNTs_x$ (x = 200, 300, 400 and 500). After 110-h test, the voltage drop of Co_3O_4/MnO_2-$CNTs_x$ increase to 1.9 V, which is attributed to the destruction of the air electrode by the migration of Zn^{2+} ions, the deposition of carbonates, and even the hydrogen evolution reaction (Fig. S15). In order to meet the requirement of high voltage and power equipment, 3-cell stack herein was designed and performed (Fig. S16). The 3-cell stack exhibits an open circuit voltage of ≈3.5 V and a high power density of 1439 mW cm^{-2} which are similar to the OCV and power densities of each cell in the 3-cell stack (Fig. S16a). The work voltage is stable without obvious attenuation (160 h) under constant-current discharged at a current density of 10 mA cm^{-2} (Fig. S16c). In addition, we can find that the decline of the 3-stack performance derives from the attenuation of the 2nd and 3rd cells (Fig. S16d). The stack also possesses remarkable charging-discharging activity (the voltage gap at a current density of 70 mA cm^{-2}: 3.32 V) and high recycling durability (540 cycles) (Fig. S16 **e** and **f**). Such exceptional performances of zinc-air batteries are attributed to the high matching of each cell of the stack as well as the high efficient ORR and OER performance of Co_3O_4/MnO_2-$CNTs_{350}$. Further, they were able to stack several electrode layers in order to achieve high capacity while maintaining flexibility.

Inspired by the excellent flexible property of all-solid-state electrolyte as well as stimulated by the increasing interests on wearable electronic devices, a flexible rechargeable laminated structure zinc-air battery is fabricated by combining AEM integrated into the zinc anode and air cathode (Fig. 3e). As shown in Fig. 3f, the flexible zinc-air batteries with the CS/EMImC-Co-EP/GO membrane present a high open-circuit voltage (OCV) of 1.227V and an outstanding power density of 83.5 mW cm^{-2}, which is approximate to that of the commercial Tokuyama A901membrane based flexible zinc-air battery (84.1 mW cm^{-2}). Discharged at a constant-current density of 5 mA cm^{-2} for 15 h, the battery with the CS/EMImC-Co-EP/GO membrane electrolyte affords no obvious voltage drop, confirming the high stability, which is superior to the commercial Tokuyama A901membrane (8 h, Fig. 3g). And the CS/EMImC-Co-EP/GO membrane delivers an obvious higher discharge capacity (~ 75 mAh) (longer discharge time) than the A901 membrane (~ 40 mAh). And the specific capacity was still ~600 mAh g^{-1}, which is normalized to the mass of consumed zinc. Particularly, the CS/EMImC-Co-EP/GO membrane is fully comparable to the commercial Tokuyama A901membrane in flexible zinc-air battery for discharge process. In charge and discharge polarization curves (Fig. S17), the CS/EMImC-Co-EP/GO membrane-based battery exhibits a high open-circuit voltage of ≈1.3 V, similar to that of the Tokuyama A901-based battery, and almost potentials change in different current densities over the A901-based battery. The pulse charge and discharge cycling performance of the flexible batteries using the CS/EMImC-Co-EP/GO and A901 membranes are also measured using a pulse cycling technique with each cycle per 10 min at a current density of 5 mA cm^{-2} (Fig. 3h). The CS/EMImC-Co-EP/GO-based battery shows a remarkable stable cycling performance advantage over the A901-based battery. The CS/EMImC-Co-EP/GO-based battery demonstrates longer cycling stability without any voltage change after 35 h; while, the A901-based battery gives a noticeable performance degradation after 22 h. The discharge and charge potentials of CS/EMImC-Co-EP/GO-based battery are 300 and 254 mV smaller than those of A901-based battery at the 25th hour. Compared to the A901 membrane, the CS/EMImC-Co-EP/GO-based battery exhibits more outstanding rechargeability and stability, which may be attributed to the smaller anisotropic swelling degree and higher water uptake. These advantages prevent electrolyte dry out and wrinkling problems, lengthen battery

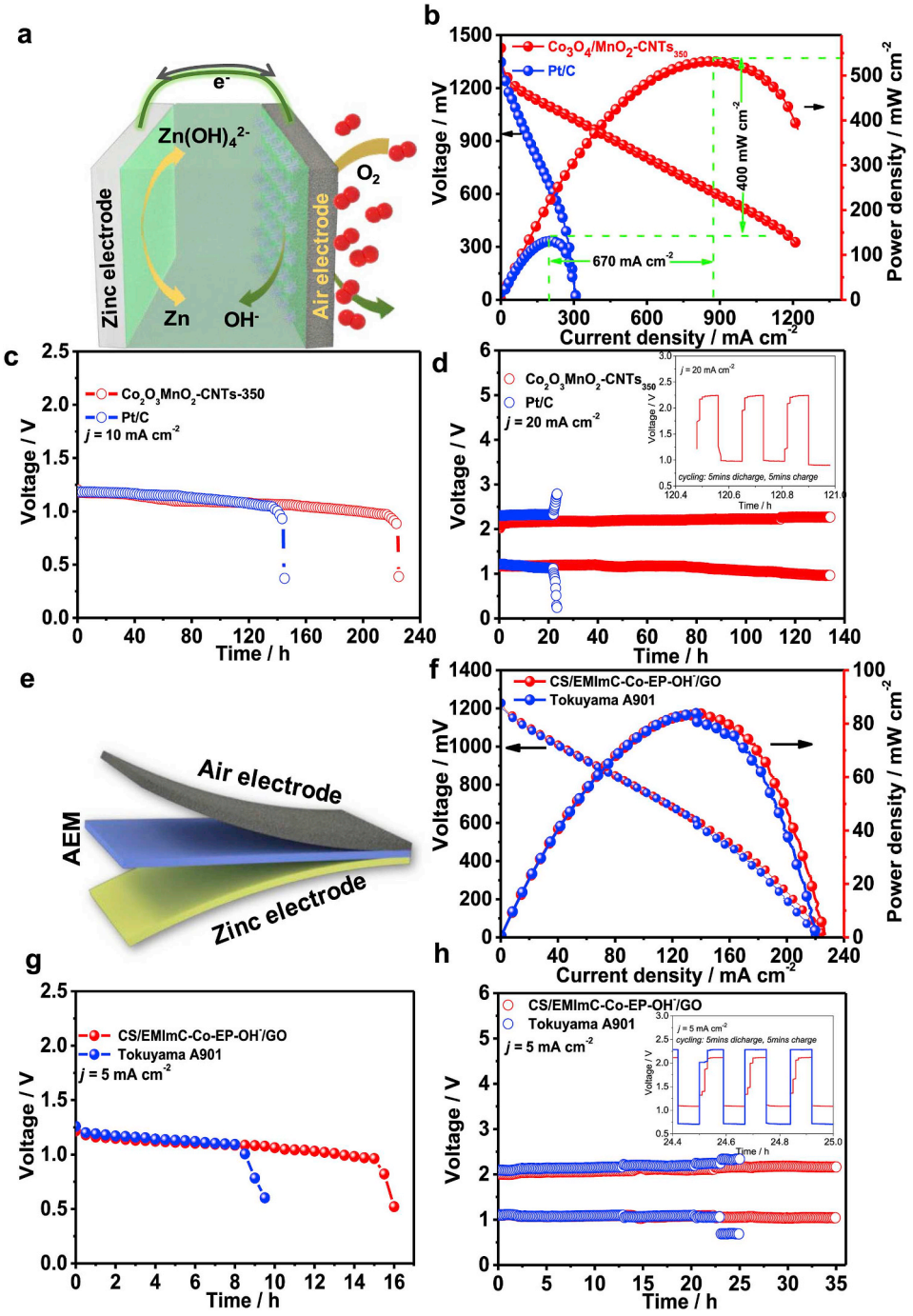

Fig. 3. (a) Illustration of the aqueous zinc-air batteries. The zinc-air battery (b) Polarization curves and corresponding power density plots; (c) Long-time discharge curves; (d) Cycling data at 20 mA cm^{-2} in cycle periods of 10 min per cycle. (e) Illustration of the flexible all-solid-state zinc-air batteries. the flexible zinc-air battery (f) Polarization curve and corresponding power density plot; (g) Long-time discharge curve; (h) Cycling data at 5 mA cm^{-2} in cycle periods of 10 min per cycle.

life, and reduce Ohmic polarization. It is known that a theoretical OCV of flexible zinc-air batteries is between 1.65 V, which is much less than that of lithium-ion batteries. While, stacking the batteries in series, such as a combination of the three flexible single cell can easily improve the inherently low working voltage of flexible zinc-air batteries, obtaining high-voltage energy and power delivery. So the flexible battery is amenable to the series designs of the flexible and all-solid-state characteristics. The flexible stack is also evaluated by using identical parameters of single flexible batteries. Compared with the single cell, the flexible stack shows almost triple discharge voltage under the identical current and delivers a high peak power of 202.1 mW cm^{-2}, and the high OCV of 3-cell stack is 3.7 V verging on lithium-ion batteries (Fig. S18a). Meanwhile, the stack affords the long-terms stability for galvanostatic discharge (13 h) and charge-discharge progress (180 cycles) (Figs. S18b–d). The 3-cell stack displays impressive performance, which is due to the high activity of the catalyst, the excellent performance of the alkaline film, and the consistency of each cell. Notably, the flexible stack can effectively avoid low efficiency and short lifetime of the charge-discharge process, which result from the cell-to-cell variation.

In general, owing to internal short circuits, existing flexible batteries suffer from serious limitations during bending. Hence, the flexible zinc-air battery was bent and investigated at the various bending angles under atmospheric air (Fig. 4a). As shown in Fig. 4b, the peak power

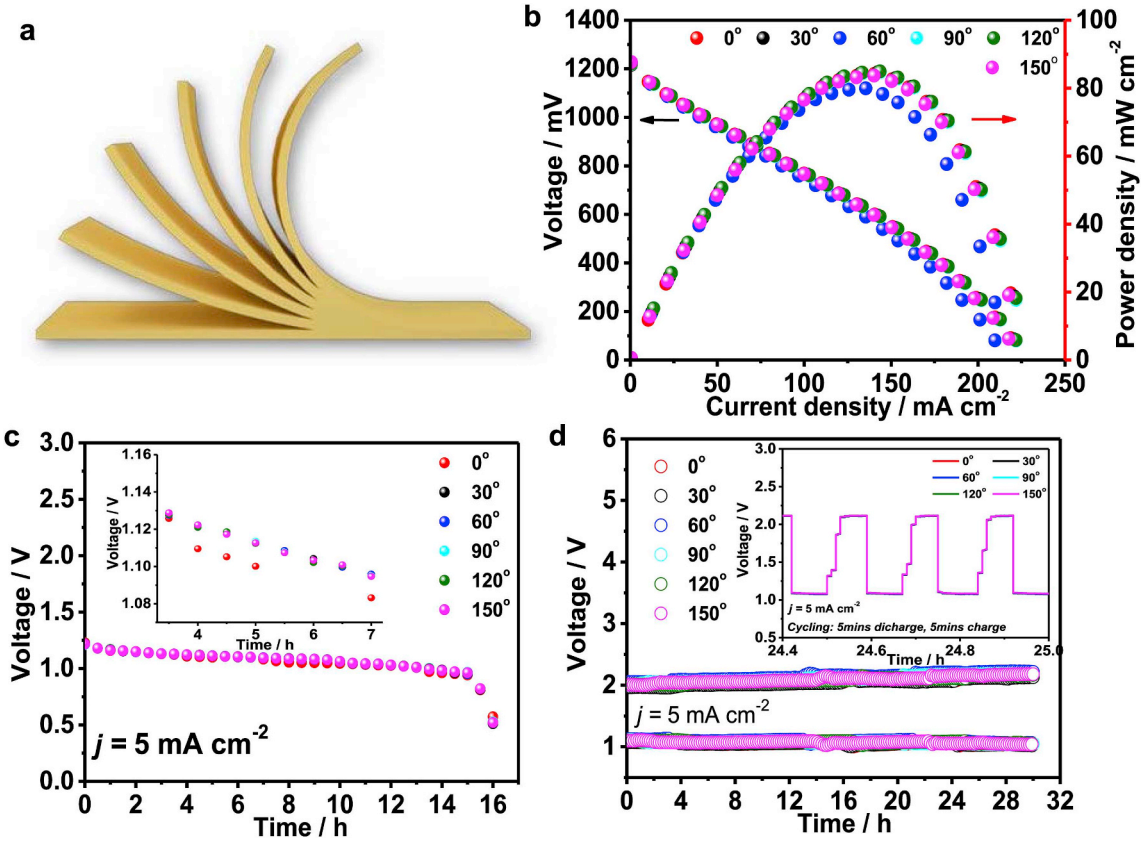

Fig. 4. (a) Illustration and practical image of the assembled flexible zinc-air battery at 0°, 30°, 60°, 90°, 120° and 150° bending angles; The performances of the flexible zinc-air battery at 0°, 30°, 60°, 90°, 120° and 150° bending angles; (b) Polarization curve and corresponding power density plots; (c) Long-time discharge curve; (d) Cycling data at 20 mA cm^{-2} in cycle periods of 10 min per cycle.

density remained virtually unchanged at 0°, 30°, 60°, 90°, 120° and 150° given bending angles. Only a minor loss of the output power density (i.e., 5 mW cm^{-2}) is observed under the bending angle of 90° (Fig. 4b), which is due to harsh bending stress lead to the electrolyte suffers from losing water. This result reveals not only a robust adhesion between the electrolyte membrane and the electrode but also the good capability of the CS/EMImC-Co-EP/GO membrane to maintain its high ionic conductivity under bending conditions. The CS/EMImC-Co-EP/GO membrane galvanostatically discharged at a current density of 5 mA cm^{-2} affords no differences in the discharge voltage profiles at various bending angles (Fig. 4c). As displayed in Fig. 4d, the flexible zinc-air battery exhibits excellent charge-discharge stability for over 180 cycles without any significant degradation of performance at any given bending angles. And the potentials of discharge and charge process under 0° remain virtually unchanged during the overall cycles and which is similar to other bending angles such as 30°, 60°, 90°, 120° and 150°. Additionally, the expanded view of the 147th cycle to 149th cycle (**the inset** of Fig. 4d) shows that the different bending angles do not affect the battery charge and discharge performance, demonstrating a linear charge-discharge voltage profile. This superior cycling stability of the cell can be attributed to its highly flexible components along with structural integrity between the electrodes and the gelled membrane. These results indicate that the different bending angles almost do not affect the flexible battery performance, proving the remarkable physically flexibility and packaging technique.

Since zinc-air batteries are open systems, the traditional electrolytes (such as 6 M KOH) are extremely sensitive to CO_2, which can form carbonates ($2KOH + CO_2 = K_2CO_3 + H_2O$ and/or $KOH + CO_2 = KHCO_3$). This phenomenon can cause a decline in electrolyte conductivity. The crystallization of carbonates in the air electrode also clogs reaction channel and decreases its activity, which directly leads to the battery performance attenuation. In order to study the influence mechanism of CO_2, the unique test was designed shown in Fig. 5a. The effect of CO_2 penetration time (0.5–20h) on the performance of the aqueous battery was investigated. As seen in Fig. S19, with the increase of CO_2 access time, the pH value of the solution decreased, the power density and the discharge time at 10 mA cm^{-2} of the battery also decreased rapidly. The pH value of the solution keep steady at 8.7 to 8.8 after 10 h, the power density of the battery is also maintained at about 22 mW cm^{-2}, and the constant current (10 mA cm^{-2}) discharging time low to about 1 h. As shown in Fig. S20 and Fig. S21, the air electrode surface is almost completely covered by K_2CO_3 or $KHCO_3$ after the CO_2 entering time up to 10 h. These phenomena prove that a number of K_2CO_3 or $KHCO_3$ crystal on the air electrode surface seriously hindered the O_2 transfer.

CO_2 is an austere threat to the operation of alkaline aqueous zinc-air batteries. But it has little impact to flexible zinc-air battery performance in theory, which is mainly due to the flexible battery using all-solid-state AEM rather than alkaline solution as electrolyte. To this end, the test of the toxicity of CO_2 for aqueous and flexible zinc-air batteries was carried out. Briefly, the battery (aqueous or flexible zinc-air batteries) continues to the previous test when it was placed in a CO_2 atmosphere over 20 h. Fig. 5b clearly shows the power density of aqueous zinc-air battery decreases rapidly under CO_2 atmosphere over 20 h, which is lower than the initial value of 534 mW cm^{-2} and higher than that of Pt/C (Fig. S22a). The discharge polarization curves and peak power density of the all-solid-state flexible battery with the hybrid exhibit negligible change (Fig. 5c), whereas the flexible battery with Pt/C shows obvious decrease (Fig. S22b). Fig. 5d displays that the discharge curve is stable under normal air condition at a current density of 10 mA cm^{-2} for 60 h. While the battery was placed in CO_2 for 20 h, the voltage has a significant reduction. Compared to the previous test (220h), the

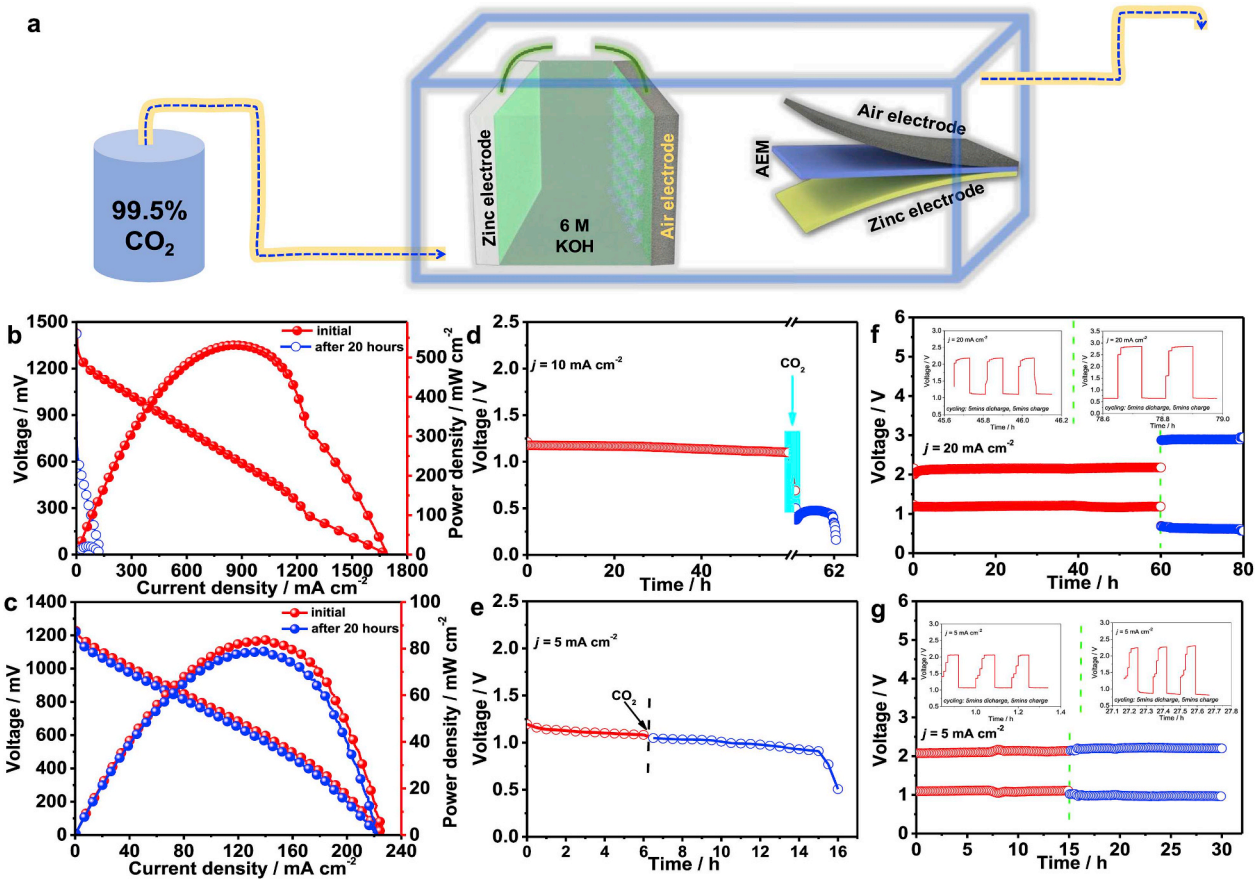

Fig. 5. (a) Schematic image of the test of the toxicity of carbon dioxide of the zinc air battery; the Polarization curve and corresponding power density plot of (b) the aqueous zinc-air batteries and (c) the flexible zinc-air batteries. Long-time discharge curve of (d) the aqueous zinc-air batteries and (e) the flexible zinc-air batteries. Cycling data at 20 mA cm^{-2} in cycle periods of 10 min per cycle of (f) the aqueous zinc-air batteries and (g) the flexible zinc-air batteries.

aqueous zinc-air battery discharge voltage dropped quickly, which arise from the formation of by K_2CO_3 and $KHCO_3$ blocking the mass transfer. Fig. 5e further shows an ideal situation for the flexible battery, presenting a stable voltage at a current density of 50 mA cm^{-2} for 6 h later. All the above results not only indicate carbon dioxide has little effect on the long time discharge of the flexible battery, but also show the high activity and strong durability of the hybrid catalyst. Moreover, the voltage drop of aqueous zinc-air battery has obvious increase from 0.89 to 3.02 V under CO_2 atmosphere after 20 h (Fig. 5f and **its inset**). Whereas, for flexible zinc-air batteries (Fig. 5g and **its inset**), the voltage of the discharge (0.96 V) and charge processes (2.19 V) maintains very well with no visible change over 30 h under CO_2 atmosphere after 20 h. In a word, all these results verify the presence of carbon dioxide is a serious threat to the traditional zinc-air battery. But the all-solid-state and flexible battery effectively solve this problem by inhibiting carbonate formation. Therefore, this new type of battery will have better commercial value and practical application prospect.

For further understanding the catalytic mechanism for ORR and OER, we constructed two models, p(3 × 2) MnO_2(110), Co_3O_4@MnO_2(110), to modelling the MnO_2(110) and Co_3O_4 loaded MnO_2(110) systems (Figs. S24 and S25). The overpotentials that characterize the catalytic activities for ORR and OER at various sites were calculated by the standard hydrogen electrode (SHE) method developed by Rossmeisl et al. [56] The detailed computational method was in the section of Computation method (see Supporting Information). The detailed adsorption free energy (△G) of O, OH, and OOH on MnO_2(110), Co_3O_4@MnO_2(110); the ΔG for each step (△G_a, △G_b, △G_c, △G_d); the overpotential (η) of ORR and OER are summarized in Table S3 and Fig. 6a–d. To understand why adding the Co_3O_4 nanoparticles to MnO_2 (110) surface, the performance towards ORR and ORE enhanced much more, we compared the overpotential of ORR and OER of surface Mn site of MnO_2(110) surface and top Co site and surface Mn sites (Mn1 and Mn2) of Co_3O_4@MnO_2(110). The reason is that after Co_3O_4 cluster loading on the MnO_2(110) surface, the neighbor Mn sites (Mn1 and Mn2) of Co_3O_4 cluster are much more activated. The ORR and OER overpotentials of the Mn1 and Mn2 are much more decreased compared pure MnO_2(110) surface (0.20, 0.24 *vs* 0.50 eV; 0.21, 0.28 *vs* 0.32 eV). It is found the top Co site of Co_3O_4 is not the active site for OER and ORR, because of its high overpotentials of ORR and OER (0.96, 0.49 eV). From the electronic view of the systems, Fig. 6e shows that the 3d states of Mn1 and Mn2 are decreased much more at the Fermi level compared that of surface Mn on pure MnO_2(110), which accounts for less activity for OH adsorption. This would be better for OH removal and reduce the ORR overpotential. Bader Charge analysis [57] and Charge density difference plot in Fig. 6f shows that Co_3O_4 transfer large amount of electrons to MnO_2(110) surfaces, about 0.86 e. The surface Mn1 and Mn2 atoms also get little electrons (about 0.1 e for each). The electrons got from Co_3O_4 fill the unoccupied states and made the Mn1, Mn2 3d density of states move forward lower energy entirely, which made the reduction of density of states at the Fermi level, evidenced by the vanish of the peak at the Fermi level of the surface Mn on pure MnO_2(110) surface. But the 3d states of Co at the Fermi level are much high, which induced the overbinding of OH, hence the difficulty for OH removal and very large ORR overpotential. At the same time, the Co_3O_4 loading on the MnO_2(110) surface, the bottom Co atoms bonded with the surface O of MnO_2(110) surface. Hence, due to the competition of bottom Co

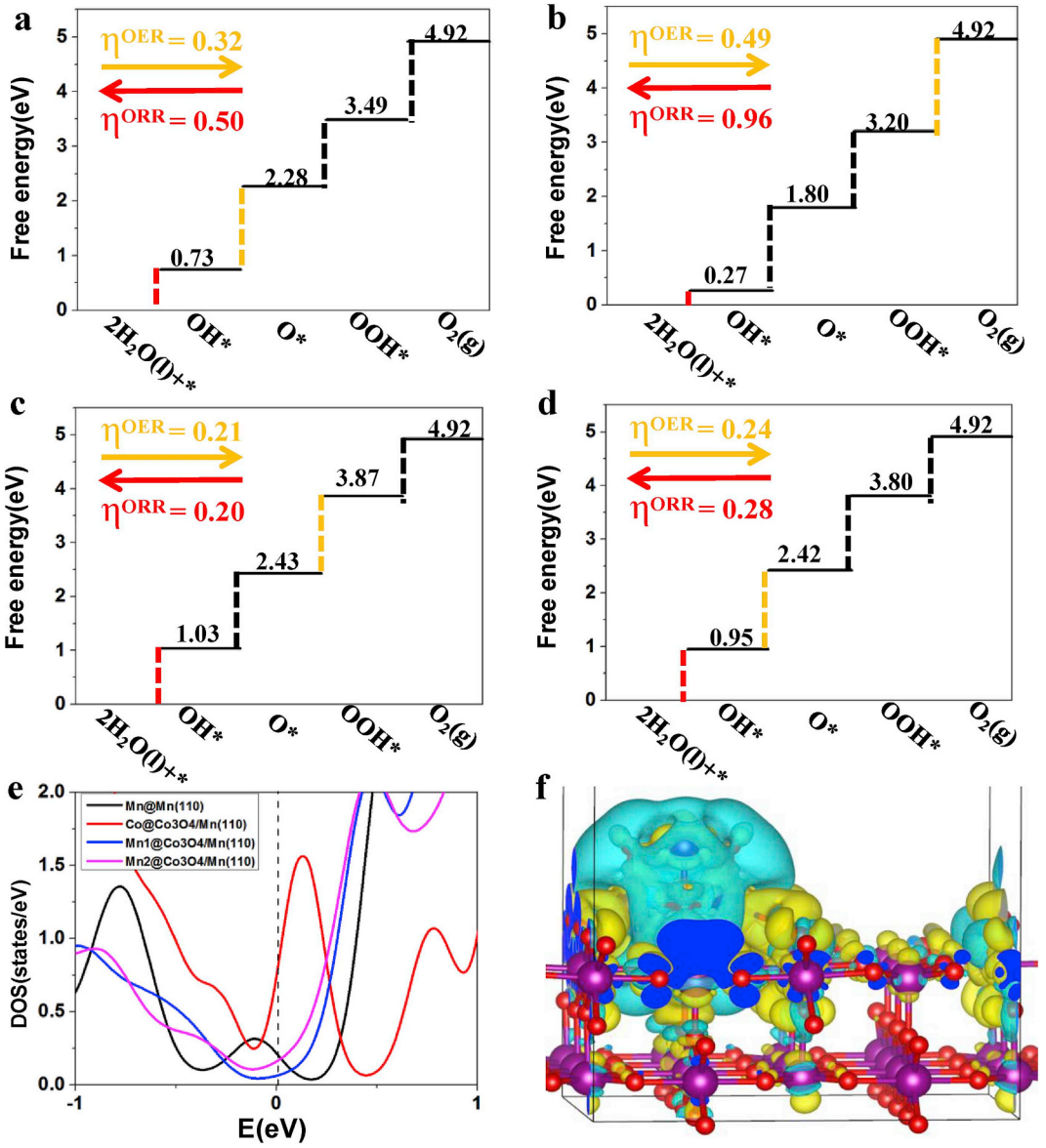

Fig. 6. (a) The free energy diagrams of OER and ORR on the surface Mn site of MnO2(110) (a), Co top site of Co3O4@MnO2(110) (b); Mn1 site of Co3O4@MnO2(110) (c); Mn2 site of Co3O4@MnO2(110) (d) at the U = 0 V. The red and the yellow dot lines are the rate limiting step for ORR and OER, respectively. (A colour version of this figure can be viewed online.); (e)The 3d density of states of surface Mn of MnO2(110), Mn1, Mn2 and top Co of Co3O4@MnO2(110) systems. (f) The charge density difference of Co3O4@MnO2(110) system. The purple, red, blue represents the Mn, O, Co respectively. Negative and positive values are represented in light blue and yellow, respectively. The isosurface value used is 0.0005 e/Å^3.

atoms, the hydrogen bonding with OH and OOH are much decreased. Correspondingly, the $\triangle G_b$($\triangle G_{O^*}$ - $\triangle G_{OH^*}$) is decreased, hence the overpotentials of OER are also decreased on the Mn1 and Mn2 sites than that of surface Mn site of pure MnO_2(110) surface. This high activity is also coincidence with our experimental results.

4. Conclusions

In summary, the selective syntheses of Co_3O_4/MnO_2-CNTs and CS/EMImC-Co-EP/GO with unique physicochemical properties have been accomplished by carefully controlling the calcined temperature and the ratio of chitosan and GO, respectively. The hybrid catalyst with abundant mesoporous structure implemented high surface area, and the AEM realized three-dimensional semi-interpenetrating network structure. The density functional theory (DFT) proves that the neighbor Mn sites (Mn1 and Mn2) of the MnO_2(110) surface are much more activated by the bottom Co atoms, further promoting the catalytic activity. The optimal balances of physicochemical properties have been found for hybrid catalyst and AEM. Based on these researches, Co_3O_4/MnO_2-CNTs display significant catalytic activity and stability for ORR, OER and aqueous zinc-air batteries. The AEM reveals high hydroxyl anion conductivity, remarkable flexibility and strong mechanical strength. Specifically, the flexible zinc-air battery and stack, which have been fabricated using Co_3O_4/MnO_2-CNTs as air electrode catalyst and CS/EMImC-Co-EP/GO as all-solid-state electrolyte, demonstrate high power/energy density, long durability, outstanding flexible property and excellent tolerance toxicity of CO_2. The work opens up a facial but effective pathway of obtaining high-performance bifunctional catalyst and AEM as promising candidates for flexible devices and electric vehicles.

Notes

The authors declare no competing financial interest.

Acknowledgments

This work was financially supported by the National Natural Science Foundation of China (21972017, U1510120), the Fundamental Research Funds for the Central Universities (2232018A3-06, CUSF-DH-D-2018075), the U.S. National Science Foundational (NSF-1747603) and Shanghai Tongji Gao Tingyao Environmental Science & Technology Development Foundation (STGEF). All the financial supports are gratefully acknowledged.

Appendix A. Supplementary data

Supplementary data to this article can be found online at https://doi.org/10.1016/j.nanoen.2019.104021.

References

[1] J. Fu, Z.P. Cano, M.G. Park, A. Yu, M. Fowler, Z. Chen, Adv. Mater. 29 (2017).
[2] Z. Liu, J. Xu, D. Chen, G. Shen, Chem. Soc. Rev. 44 (2015) 161–192.
[3] S. Mao, Z. Wen, T. Huang, Y. Hou, J. Chen, Energy Environ. Sci. 7 (2014) 609–616.
[4] B.-Q. Li, S.-Y. Zhang, B. Wang, Z.-J. Xia, C. Tang, Q. Zhang, Energy Environ. Sci. 11 (2018) 1723–1729.
[5] J. Zhang, Z. Zhao, Z. Xia, L. Dai, Nat. Nanotechnol. 10 (2015) 444–452.
[6] C. Tang, H.-F. Wang, J.-Q. Huang, W. Qian, F. Wei, S.-Z. Qiao, Q. Zhang, Electrochem. Energy Rev. 2 (2019) 332–371.
[7] Y.-J. Wang, B. Fang, D. Zhang, A. Li, D.P. Wilkinson, A. Ignaszak, L. Zhang, J. Zhang, Electrochem. Energy Rev. 1 (2018) 1–34.
[8] F. Meng, H. Zhong, D. Bao, J. Yan, X. Zhang, J. Am. Chem. Soc. 138 (2016) 10226–10231.
[9] J. Fu, D.U. Lee, F.M. Hassan, L. Yang, Z. Bai, M.G. Park, Z. Chen, Adv. Mater. 27 (2015) 5617–5622.
[10] D.U. Lee, P. Xu, Z.P. Cano, A.G. Kashkooli, M.G. Park, Z. Chen, J. Mater. Chem. A 4 (2016) 7107–7134.
[11] X. Liu, M. Park, M.G. Kim, S. Gupta, G. Wu, J. Cho, Angew. Chem. 54 (2015) 9654–9658.
[12] L. Ma, S. Chen, Z. Pei, Y. Huang, G. Liang, F. Mo, Q. Yang, J. Su, Y. Gao, J.A. Zapien, C. Zhi, ACS Nano 12 (2018) 1949–1958.
[13] F. Cheng, J. Chen, Chem. Soc. Rev. 41 (2012) 2172–2192.
[14] Y. Li, H. Dai, Chen, Chem. Soc. Rev. 43 (2014) 5257–5275.
[15] Y. Liang, Y. Li, H. Wang, J. Zhou, J. Wang, T. Regier, H. Dai, Nat. Mater. 10 (2011) 780–786.
[16] Y. Gorlin, T.F. Jaramillo, J. Am. Chem. Soc. 132 (2010) 13612–13614.
[17] N. Xu, Y. Liu, X. Zhang, X. Li, A. Li, J. Qiao, J. Zhang, Sci. Rep. 6 (2016) 33590.
[18] M. Yu, Z. Wang, C. Hou, Z. Wang, C. Liang, C. Zhao, Y. Tong, X. Lu, S. Yang, Adv. Mater. 29 (2017).
[19] X. Chen, B. Liu, C. Zhong, Z. Liu, J. Liu, L. Ma, Y. Deng, X. Han, T. Wu, W. Hu, J. Lu, Adv. Energy Mater. 7 (2017) 1700779.
[20] S. Peng, X. Han, L. Li, S. Chou, D. Ji, H. Huang, Y. Du, J. Liu, S. Ramakrishna, Adv. Energy Mater. 8 (2018) 1800612.
[21] J. Fu, F.M. Hassan, C. Zhong, J. Lu, H. Liu, A. Yu, Z. Chen, Adv. Mater. 29 (2017).
[22] N. Xu, Y. Zhang, T. Zhang, Y. Liu, J. Qiao, Nano Energy 57 (2019) 176–185.
[23] J. Park, M. Park, G. Nam, J.S. Lee, J. Cho, Adv. Mater. 27 (2015) 1396–1401.
[24] M. Wang, N. Xu, J. Fu, Y. Liu, J. Qiao, J. Mater. Chem. A 7 (2019) 11257–11264.
[25] J. Zhang, J. Fu, X. Song, G. Jiang, H. Zarrin, P. Xu, K. Li, A. Yu, Z. Chen, Adv. Energy Mater. 6 (2016) 1600476.
[26] F. Song, Y. Fu, Y. Gao, J. Li, J. Qiao, X.-D. Zhou, Y. Liu, Electrochim. Acta 177 (2015) 137–144.
[27] N. Xu, J. Qiao, X. Zhang, C. Ma, S. Jian, Y. Liu, P. Pei, Appl. Energy 175 (2016) 495–504.
[28] G. Du, X. Liu, Y. Zong, T.S. Hor, A. Yu, Z. Liu, Nanoscale 5 (2013) 4657–4661.
[29] Z.Q. Liu, H. Cheng, N. Li, T.Y. Ma, Y.Z. Su, Adv. Mater. 28 (2016) 3777–3784.
[30] M.G. Park, D.U. Lee, M.H. Seo, Z.P. Cano, Z. Chen, Small 12 (2016) 2707–2714.
[31] N. Xu, J. Qiao, Q. Nie, M. Wang, H. Xu, Y. Wang, X.-D. Zhou, Catal. Today 318 (2017) 144–149.
[32] W. Xu, W. Xie, Y. Wang, ACS Appl. Mater. Interfaces 9 (2017) 28642–28649.
[33] X. Zhang, H. Xu, X. Li, Y. Li, T. Yang, Y. Liang, ACS Catal. 6 (2015) 580–588.
[34] S. Khalid, C. Cao, M. Naveed, W. Younas, Sustainable Energy & Fuels 1 (2017) 1795–1804.
[35] Y. He, J. Zhang, G. He, X. Han, X. Zheng, C. Zhong, W. Hu, Y. Deng, Nanoscale 9 (2017) 8623–8630.
[36] Z. Zhang, F. Xiao, J. Xiao, S. Wang, J. Mater. Chem. A 3 (2015) 11817–11823.
[37] S.K. Singh, V.M. Dhavale, S. Kurungot, ACS Appl. Mater. Interfaces 7 (2015) 21138–21149.
[38] M. Kuang, Q. Wang, H. Ge, P. Han, Z. Gu, A.M. Al-Enizi, G. Zheng, ACS Energy Lett 2 (2017) 2498–2505.
[39] Y.-P. Deng, Y. Jiang, D. Luo, J. Fu, R. Liang, S. Cheng, Z. Bai, Y. Liu, W. Lei, L. Yang, J. Zhu, Z. Chen, ACS Energy Lett 2 (2017) 2706–2712.
[40] S.S. Shinde, C.H. Lee, A. Sami, D.H. Kim, S.U. Lee, J.H. Lee, ACS Nano 11 (2017) 347–357.
[41] X. Qiao, S. Liao, R. Zheng, Y. Deng, H. Song, L. Du, ACS Sustain. Chem. Eng. 4 (2016) 4131–4136.
[42] A. Indra, P.W. Menezes, N.R. Sahraie, A. Bergmann, C. Das, M. Tallarida, D. Schmeisser, P. Strasser, M. Driess, J. Am. Chem. Soc. 136 (2014) 17530–17536.
[43] W. Yan, Z. Yang, W. Bian, R. Yang, Carbon 92 (2015) 74–83.
[44] S. Liu, W. Bian, Z. Yang, J. Tian, C. Jin, M. Shen, Z. Zhou, R. Yang, J. Mater. Chem. A 2 (2014) 18012–18017.
[45] W. Yan, X. Cao, J. Tian, C. Jin, K. Ke, R. Yang, Carbon 99 (2016) 195–202.
[46] M. Prabu, P. Ramakrishnan, P. Ganesan, A. Manthiram, S. Shanmugam, Nano Energy 15 (2015) 92–103.
[47] Y. Cheng, S. Dou, J.-P. Veder, S. Wang, M. Saunders, S.P. Jiang, ACS Appl. Mater. Interfaces 9 (2017) 8121–8133.
[48] G. Li, X. Wang, J. Fu, J. Li, M.G. Park, Y. Zhang, G. Lui, Z. Chen, Angew. Chem. 55 (2016) 4977–4982.
[49] N. Ma, Y. Jia, X. Yang, X. She, L. Zhang, Z. Peng, X. Yao, D. Yang, J. Mater. Chem. A 4 (2016) 6376–6384.
[50] X. Han, F. Cheng, T. Zhang, J. Yang, Y. Hu, J. Chen, Adv. Mater. 26 (2014) 2047–2051.
[51] Z. Pei, Y. Huang, Z. Tang, L. Ma, Z. Liu, Q. Xue, Z. Wang, H. Li, Y. Chen, C. Zhi, Energy Storage Mater 20 (2019) 234–242.
[52] H. Li, L. Ma, C. Han, Z. Wang, Z. Liu, Z. Tang, C. Zhi, Nano Energy 62 (2019) 550–587.
[53] D.S. Kim, G.P. Robertson, Y.S. Kim, M.D. Guiver, Macromolecules 42 (2009) 957–963.
[54] B. Lin, L. Qiu, J. Lu, F. Yan, Chem. Mater. 22 (2010) 6718–6725.
[55] H. Ma, B. Wang, RSC Adv. 4 (2014) 46084–46092.
[56] J. Rossmeisl, Z.W. Qu, H. Zhu, G.J. Kroes, J.K. Nørskov, J. Electroanal. Chem. 607 (2007) 83–89.
[57] G. Henkelman, A. Arnaldsson, H. Jónsson, Comput. Mater. Sci. 36 (2006) 354–360.

Dr. Nengneng Xu received his BS degree in Chemical Engineering and Technology (with Prof. Dingxing Tang) from Anhui Polytechnic University in 2014. He completed his MS degree in Donghua University in 2016. After that, He received his Ph.D. degree from Donghua University under the supervision of Prof. Jinli Qiao. He is spending one year (2017–2018) as a visiting scholar in the University of Louisiana at Lafayette with Prof. Xiao-Dong Zhou. His current research focuses on the development of nanostructured catalysts for rechargeable metal-air batteries and methane oxidation.

Dr. Yanxing Zhang is an Associate professor of college of physics and materials science at Henan normal university. He received his PhD in Condense matter physics at Henan normal university in 2016. In 2015, he has visited Professor Ruqian Wu's Group and worked with Wilson ho's group in University of California Irvine for one year to do theoretical modelling of STM experiments. His current research activities include theoretical studies aimed at the development of high efficient, low cost, green oxygen reduction reaction (ORR), oxygen evolution reaction (OER), hydrogen evolution reaction (HER) catalysis, and sulfur, carbon tolerant solid oxide fuel cell (SOFC) anode materials.

Dr. Min Wang obtained her M.S. in Light Industry Technology and Engineering from Qingdao University of Science and Technology, Qingdao, Shandong Province, China. At present, she completed her Ph.D. degree under the supervision of Prof. Jinli Qiao from the College of Environmental Science and Engineering of Donghua University in 2019, Shanghai, China. Her research topic mainly focuses on the design and fabrication of alkaline anion exchange membrane for use in energy storage and conversion devices.

Dr. Xiujun Fan studied microelectronics and solid state electronics and obtained his Ph.D. from Beijing University of Technology in 2015. Since 2015 he has been full professor at Shanxi University. Dr. Fan was a recipient of the Shanxi Excellent Young Scholar Grant (2018). He has over 30 research publications, including 2 highly cited ESI papers. Dr. Fan also has over 20 patents about low-dimensional nanomaterial, electrochemical conversion, electrocatalysis and energy storage. His current research interests cover nanostructured films, renewable energy generation and storage, and smart/flexible electronics, with a particular focus on advanced materials and their electrochemical applications.

Dr. Tao Zhang is a Professor at Shanghai Institute of Ceramics, Chinese Academy of Sciences (SICCAS). He received his Ph.D. from Fudan University in 2007, then an associate professor at Shanghai University. From 2008 to 2015, he worked as a research scientist at Mie University, then a research fellow at the National Institute of Advanced Industrial Science and Technology (AIST), Japan. He was conferred “Hundred Talents” title from the Chinese Academy of Sciences in 2015. His current research interests focus on the area of advanced energy electrochemistry, including the devices and the associated materials for energy conversion and storage including Li-air batteries, Li-sulfur batteries, all-solid-state polymer Li-ion batteries, and Li-ion conducting materials.

Luwei Peng received his BS degree in College of Civil Engineering and Mechanics from Xiangtan University in 2017. He finished his MS degree under the supervision of Prof. Jinli Qiao in Donghua University at 2018. Currently, he is a Ph.D. candidate at the college of Environmental Science and Engineering in Donghua University supervised by Prof. Jinli Qiao. His research direction is mainly focused on the design of transition metal nanomaterials for rechargeable metal-air batteries and electrochemical reduction of CO_2.

Dr. Xiao-Dong Zhou is the Stuller Endowed Chair and Director of the Institute for Materials Research and Innovation at the University of Louisiana at Lafayette. He received his PhD in Ceramic Engineering from University of Missouri-Rolla in 2001. His research interest is to investigate the durability of materials and interfaces for fuel cells and batteries, as well as the electrochemical activation of small molecules.

Dr. Jinli Qiao is a Professor at Donghua University, China. She received her PhD in Electrochemistry from Yamaguchi University, Japan in 2004. Then she joined the National Institute of Advanced Industrial Science and Technology (AIST) as a research fellow. Dr. Qiao has more than 20 years of scientific research experience. As the first author and corresponding author, she has published over 100 research papers in peer-reviewed journals, 4 co-authored/edited books/10 book chapters, and more than 30 Japan/China granted invention patents. Her current research interests include PEM fuel cells, metal–air batteries, all-solid-state superior capacitors and CO_2 electroreduction.